Applied Physics A (2020)126:528
https://doi.org/10.1007/s00339-020-03713-0

Applied Physics A
Materials Science & Processing

Mixing amorphous carbon enhanced electrochemical performances of $NiCo_2O_4$ nanoparticles as anode materials for sodium-ion batteries

Hung H. Nguyen[1] · Nguyen V. To[3,4] · Thu V. Tran[2] · Ky V. Nguyen[2] · Son T. Luong[2] · Nga N. T. Nguyen[1] · Chung V. Hoang[5] · Hieu S. Nguyen[5] · Nghia V. Nguyen[6]

Received: 11 March 2020 / Accepted: 8 June 2020

Abstract
The $NiCo_2O_4$ ternary transition metal oxide (NCO) has been received a great interest as anode material for sodium-ion batteries, recently. Here we show that a composite material composed of NCO nanoparticles (NCO-NPs) and amorphous carbon (NCO/C composite) displayed a superior electrochemical performance over the NCO-NPs. The NCO-NPs delivered a capacity of 172 mAh g^{-1} at the current density of 50 mA g^{-1}, and the capacity was reduced to 29 mAh g^{-1} after 50 cycles. The NCO/C composite showed a capacity of 213 mAh g^{-1} at 50 mA g^{-1}; the capacity was lowered to 119 mAh g^{-1} after 100 cycles. The capacity of the composite at 100 mA g^{-1}, 200 mA g^{-1} and 300 mA g^{-1} was ca. 123 mAh g^{-1}, 93 mAh g^{-1} and 62 mAh g^{-1}, respectively. This improvement is ascribed to the presence of the activated hard carbon of high electronic conductivity. Our work suggests that the combination of amorphous carbon with the NCO-NPs can serve as anodes for sodium-ion batteries.

Keywords Nanofabrication · Surface modification and applications · Nanomaterials · Sodium-ion battery · Anode materials · Amorphous carbon

1 Introduction

Sodium-ion batteries (SIBs) have emerged as a promising candidate to replace the lithium-ion batteries (LIBs) in the large-scale energy storage systems due to the high abundance and low cost of sodium compared with lithium. A numerous number of cathodes such as P2-type Fe-/Mn-based layered structure [1], sodium (Na) super ionic conductor (NASICON) [2], $Na_{0.44}MnO_2$ tunnel structure [3], metal oxides [4], olivine structure [5], etc. have shown their applicability to both SIBs and LIBs. In the case of anode materials, however, many materials have been served well as anodes for the LIBs but are practically electrochemical inactive for the SIBs. For example, graphite has been used as the anode material in most commercial LIBs, but it cannot be utilized for the SIBs because the Na^+ ions are hardly intercalated into the space between carbon layers in graphite [6]. Similarly, silicon and germanium, the popular anode materials for LIBs, have similar limited Na^+ ions storage [7]. On the contrary, hard carbon shows very limited redox reactivity in the LIBs, but they are electrochemically active in the SIBs [8, 9]. The anode materials for SIBs have been investigated, such as TiO_2 [10], $Na_2Ti_3O_7$ [11], $LiTi_2(PO_4)_3$ [12], hard carbon [13], graphene [14], MoS_2 [15], and vanadium-based oxides [16].

Recently, $NiCo_2O_4$ ternary transition metal oxide has been reported as promising anode materials for SIBs. For example, spindle-shaped $NiCo_2O_4$ core–shell nanostructures

✉ Nghia V. Nguyen
nghianv@hau.edu.vn

1 Hung Vuong University, Viet Tri, Phu Tho 290000, Vietnam

2 Department of Chemical Physics, Le Qui Don Technical University, 236 Hoang Quoc Viet, Cau Giay, Hanoi 100000, Vietnam

3 Institute of Research and Development, Duy Tan University, Danang 550000, Vietnam

4 The Faculty of Environmental and Chemical Engineering, Duy Tan University, Danang 550000, Vietnam

5 Institute of Materials Science, Vietnam Academy of Science and Technology, 18 Hoang Quoc Viet Street, Cau Giay District, Hanoi 100000, Vietnam

6 Research Center of Advanced Materials and Applications, Institute of Architecture, Construction, Urban, and Technology, Hanoi Architectural University, Hanoi 100000, Vietnam

Published online: 15 June 2020

showed a capacity of approximately 400 mAh g^{-1} after 100 cycles at the current density of 100 mAh g^{-1} [17]; $NiCo_2O_4$ double-shelled hollow spheres had a reversible specific capacity of 511 mAh g^{-1}, and the capacity of the material retained about 66% of its initial value after 100 cycles [18]. Hollow $NiCo_2O_4$ nanoboxes had an excellent first discharge capacity of 826 mAh g^{-1}; the capacity then rapidly decreased to 328 mAh g^{-1} after 30 cycles [19]. $NiCo_2O_4$ nanowire arrays revealed the first capacity of 542 mAh g^{-1} at the current density of 50 mA g^{-1}. The capacity retention was 81% after 50 cycles [20].

Amorphous carbon has excellent performances as anode material for SIBs. The amorphous (glassy) carbon shows a specific capacity of 338 mAh g^{-1}, which reduced to 173 mAh g^{-1} after 100 cycles [21]. The capacity of activated amorphous carbon with high porosity cycled at a current density of 0.5 A g^{-1} reaches the value of 479.2 mAh g^{-1}, which retains 96% after 150 cycles [22]. A combination of $Mo_{0.91}W_{0.09}S_2$ ultrathin nanosheets and amorphous carbon used as anode material for LIBs achieves an extremely high capacity of 1099.4 mAh g^{-1} at the second cycle with the capacity retention of 86.5% after 50 cycles [23]. More interestingly, it has been reported that nanocomposites of amorphous carbon and $Na_3V_2(PO_4)_3$-based anode material could deliver very stable capacities (approximately 100 mAh g^{-1}) during 10000 cycle of charge/discharge even at an ultrahigh current density (100 C) [24–26]. These results suggest that a combination of amorphous carbon with other anode materials could improve the electrochemical properties of the anodes for SIBs.

In this work, the $NiCo_2O_4$ nanoparticles and its combination with amorphous carbon (NCO/C) have been fabricated and investigated as anode materials for SIBs. The combination of amorphous carbon and $NiCo_2O_4$ is expected to improve the conductivity of the $NiCo_2O_4$ anode. In addition, the present of an amorphous carbon matrix between $NiCo_2O_4$ also could help to decrease the pulverization of the $NiCo_2O_4$ anode which is caused by the volume change of $NiCo_2O_4$ during charge/discharge. As a result, the electrochemical characteristics of NCO/C composite were enhanced compared to those of NCO-NPs.

2 Experimental

2.1 Synthesis and characterization of the NCO-NPs and NCO/C composite

The NCO-NPs were synthesized via solvothermal method by dissolving stoichiometric amounts of cobalt (II) chloride hexahydrate ($CoCl_2.6H_2O$), nickel (II) chloride hexahydrate ($NiCl_2{\cdot}6H_2O$), and 0.9 g urea ($CO(NH_2)_2$) (Shanghai Aladdin Bio-Chem Technology Co. Ltd., analytical grade) into 75 ml of deionized water. The mixed solution was transferred to a 150-ml autoclave and heated at 120 °C for 6 h. Then, let it cool to room temperature; the precipitated product was washed repeatedly with deionized water and ethanol. The product was collected and marked as the NCO precursor for the next uses. The NCO precursor was heated at 300 °C for 2 h in air and finally calcined at 600 °C for 1 h in argon to get the desired NCO-NPs.

The NCO/C composite was synthesized using 0.5 g of the NCO precursor and 1 g of saccharose ($C_{12}H_{22}O_{11}$) (Shanghai Aladdin Bio-Chem Technology Co. Ltd., analytical grade) as the carbon resource. The saccharose was firstly preheated at 180 °C for 10 min to become molten; then, the NCO precursor was added and rapidly stirred to form a homogeneous gel. The gel was heated at 300 °C for 2 h in air and calcined at 600 °C for 1 h in argon to obtain the NCO/C composite. The same procedure was applied on saccharose to obtain hard carbon as a reference material. The hard carbon powder was manually ground by agate mortar for at least 30 min and finally ball milled for 6 h by a planetary ball mill using a zirconium oxide ball mill jar (at 10:1 ball to powder weight ratio). The speed of main rotating disk was set at 400 rpm.

The crystal structure of the NCO-NPs and NCO/C composite was analyzed using X-ray diffraction (XRD, D-5000 SIEMEN, Cu Kα radiation, $\lambda = 1.5406$ Å). The diffraction angle (2θ) scanned range was from 10° to 70° at a step of 0.03°/s. The scanning electron microscopy (SEM) and energy-dispersive X-ray spectroscopy (EDS) images of the materials were taken by a JEOL, JSM-6490 scanning electron microscope. Thermogravimetric (TG) analysis was conducted in air from 50 to 900 °C by a Pyris 6 thermogavimetric analyzer (Perkin Elmer Inc.). Raman spectra were collected by a HORIBA Jobin–Yvon LabRAM HR Raman system using Nd:YAG laser with a wavelength of 532 nm.

2.2 Electrochemical measurements

The electrochemical tests were conducted using CR2032-type coin cells. The cells were assembled in an argon-filled glove box with moisture and oxygen concentrations less than 1.0 ppm. The active materials (NCO-NPs and NCO/C composite), conductive carbon black (super P, Alfa Aesar, 99 + %), and the binder polyvinylidene fluoride (PVDF, Alfa Aesar) with a weight ratio of 8:1:1 were mixed in N-methyl-2-pyrrolidone (Alfa Aesar, 99 + %) solvent to form a homogeneous slurry, which was then coated on a 15-μm-thick Al foil using doctor blade technique. The tape was dried in a vacuum oven at 100 °C for 24 h and pressed to get a uniform thickness sheet. The sheet was cut into circles with a diameter of 16 mm to fit into the CR2032 coin cell. Pure sodium foil (Acros Organic) was used as the negative electrode. Polypropylene (PP, TOB New Energy) was used as the separator. The electrolyte was 1 M $NaClO_4$ in a mixture of

ethylene carbonate and diethylene carbonate (EC/DEC) (1:1, in volume). The electrochemical impedance spectroscopy (EIS) and cyclic voltammetry (CV) analyses were conducted on a Metrohm Autolab (PGSTAT 302 N). The galvanostatic charge/discharge tests were taken on a NEWARE battery tester.

3 Results and discussion

The crystalline structure of the synthesized NCO-NPs and NCO/C composite was identified by X-ray diffraction measurements (Fig. 1a). All the diffraction peaks of the NCO-NPs and NCO/C composite can be well assigned to the standard pattern of the cubic spinel $NiCo_2O_4$ phase, space group Fd $\bar{3}m$ (JCPDS # 73-1702) [17, 27]. The lattice parameters and unit cell volume of the NCO-NPs and NCO/C composite are calculated using the unit cell software and listed in Table 1. The diffraction peaks corresponding to Miller index planes (220), (511), and (440) observed in the NCO-NPs' XRD pattern were disappeared in the XRD pattern of the NCO/C composite, meaning that the presence of the carbon resource affected the crystallization process of NCO phase.

Park et al. reported a small increase in the lattice parameter of the carbon-coated $Na_{2/3}Fe_{1/2}Mn_{1/2}O_2$ material possibly due to an increase in repulsion between oxygen layers caused by the decrease in Na [28]. In this work, however, a small decrease in the lattice parameters and unit cell volume of the NCO/C composite in comparison with NCO was observed. This phenomenon may be explained by the larger size of NCO particles in NCO/C composite than pure NCO powder [29], as will be observed later on. The presence of carbon also caused the NCO/C composite crystals to prefer growing (311) and (400) planes. There were no additional peaks to the XRD patterns of the NCO-NPs and NCO/C composite suggesting that crystal of a pure $NiCo_2O_4$ phase was obtained in both materials and the carbon in the NCO/C composite was amorphous.

Table 1 Lattice parameters and unit cell volume of the $NiCo_2O_4$ nanoparticles and $NiCo_2O_4$-amorphous carbon composite

Materials	Lattice parameters (Å)	Unit cell volume (Å^3)
$NiCo_2O_4$	8.0923	529.9188
$NiCo_2O_4$/C	8.0442	520.5250
JCPDS # 73-1702	8.114	534.3988

Figure 1b shows the Raman spectra of hard carbon, NCO/C composite, and NCO nanoparticles. The Raman spectrum of the NCO nanoparticles showed four distinct peaks at 182.5, 457, 502, and 649 cm^{-1} which could be assigned to the F_{2g}, E_g, F_{2g}, and A_{1g} vibration modes of the $NiCo_2O_4$ spinel structure [30]. The Raman spectrum of the hard carbon displayed two peaks at 1348 and 1580 cm^{-1} which could be ascribed to the disorder-allowed zone-edge mode of graphite (D-band) and the E2g zone-center mode of crystalline graphite (G-band), respectively [31]. The calculated integrated intensity ratio I_D/I_G of the hard carbon and the NCO/C composite is 3.21 and 2.79, respectively. These high values of I_D/I_G ratio revealed that the carbon compositions were governed by amorphous phase.

The thermal stability of the two materials is investigated and presented in Fig. 1c. The TG curve of the NCO-NPs material (red line) shows almost no weight loss when the temperature increased to 700 °C, which means the structure of NCO-NPs was stable and the material did not absorb moisture. The TG curve of the NCO/C composite (black line) illustrates that when the temperature increased to 100 °C, the curve shows an initial 2% weight loss, which is corresponded to the evaporation of moisture. The second (~44.47%) weight loss happened when the temperature increased from 400 to 500 °C can be attributed to the amorphous carbon burning.

Figure 2 shows the SEM images (a, b), TEM images (c, d), the area investigated by EDS (e), and EDS spectrum (f)

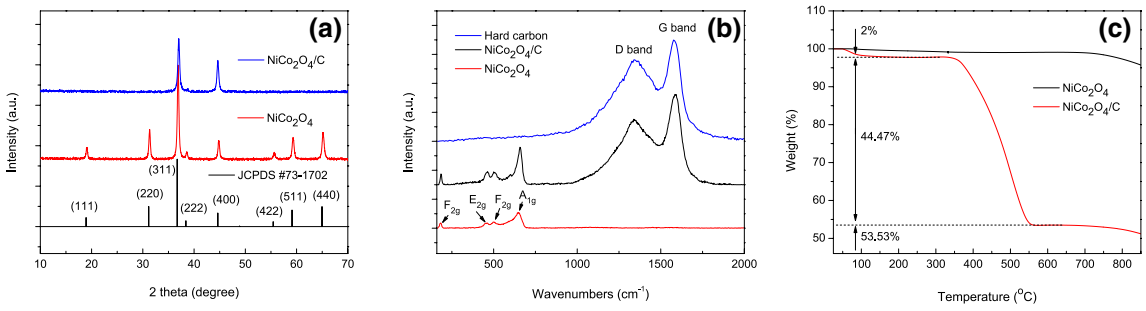

Fig. 1 **a** X-ray diffraction patterns of the $NiCo_2O_4$ nanoparticles and $NiCo_2O_4$-amorphous carbon composite, **b** Raman spectra of $NiCo_2O_4$ nanoparticles, $NiCo_2O_4$-amorphous carbon composite, and hard carbon, **c** TG curves of the $NiCo_2O_4$ nanoparticles and $NiCo_2O_4$-amorphous carbon composite

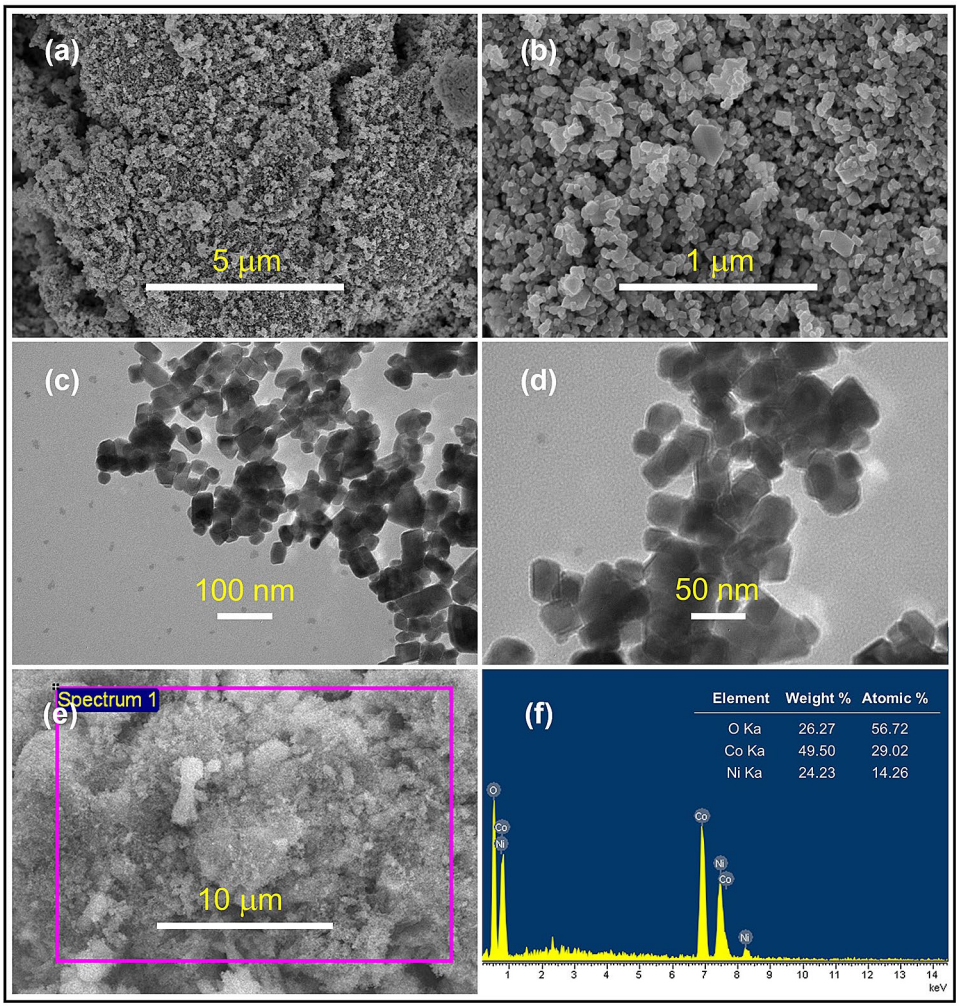

Fig. 2 **a**, **b** SEM images, **c**, **d** TEM images, **e** EDS selected area, **f** EDS spectrum of the $NiCo_2O_4$ nanoparticles

of the NCO-NPs. The NCO-NPs were porous (Fig. 2a, b, e), and the NCO-NPs had size from 30 to 100 nm (Fig. 2c, d). The EDS spectrum (Fig. 2f) shows that the NCO structure consisted of Ni, Co, and O elements. The inset of Fig. 2f shows that the atomic percentage of Ni, Co, and O elements was 14.26%, 29.02%, and 56.72%, respectively, corresponding to a Ni:Co:O atomic ratio of approximately 1:2.04:3.98. This indicates that the final NCO product was closed to the desired $NiCo_2O_4$ phase. The EDS results reconfirmed a good stoichiometry of $NiCo_2O_4$.

The morphology and the EDS spectrum of the NCO/C composite are illustrated in Fig. 3. As can be seen, the NCO particles were mixed with amorphous carbon (Fig. 3a–d). The NCO particle size in the NCO/C composite was approximately 50 nm to 150 nm, and these particles were larger than the particles in pure NCO powder (Fig. 3b). Due to the NCO precursor was mixed with hot melted saccharose, high viscosity of the melted saccharose caused an agglomeration of the NCO precursor during stirring, leading to the agglomeration of NCO particles. Figure 3e, f shows the EDS selected area and the EDS spectrum of the NCO/C composite sample that indicated the presence of Ni, Co, O, and C elements.

In order to evaluate the sodium intercalation and de-intercalation processes, the NCO-NPs and NCO/C composite were used as the electrodes of CR2032 half cells and electrochemical measurements were carried out. Figure 4a shows the first, second, and third typical CV curves of the NCO-NPs at a scan rate of 0.2 mV s^{-1}, measured between 0 and 3 V. The shapes of initial three CV curves are similar (except the intensity of the redox peaks), indicating that the sodium-ion storage processes of the first three cycles were the same. The redox peak intensities decreased from the first to the third cycle suggesting that the capacity of the NCO-NPs had been decreased, which indicates a moderated cycle ability of the NCO-NPs [32, 33]. The Li insertion and extraction reactions into/from NCO materials have been reported in the literature [34–37]. It is believed that the Na ion storage mechanism in the NCO material is theoretically similar to that of the Li ion storage; the Na intercalation and de-intercalation reactions in the NCO-NPs and NCO/C composite were possibly taken as follows [19, 20]:

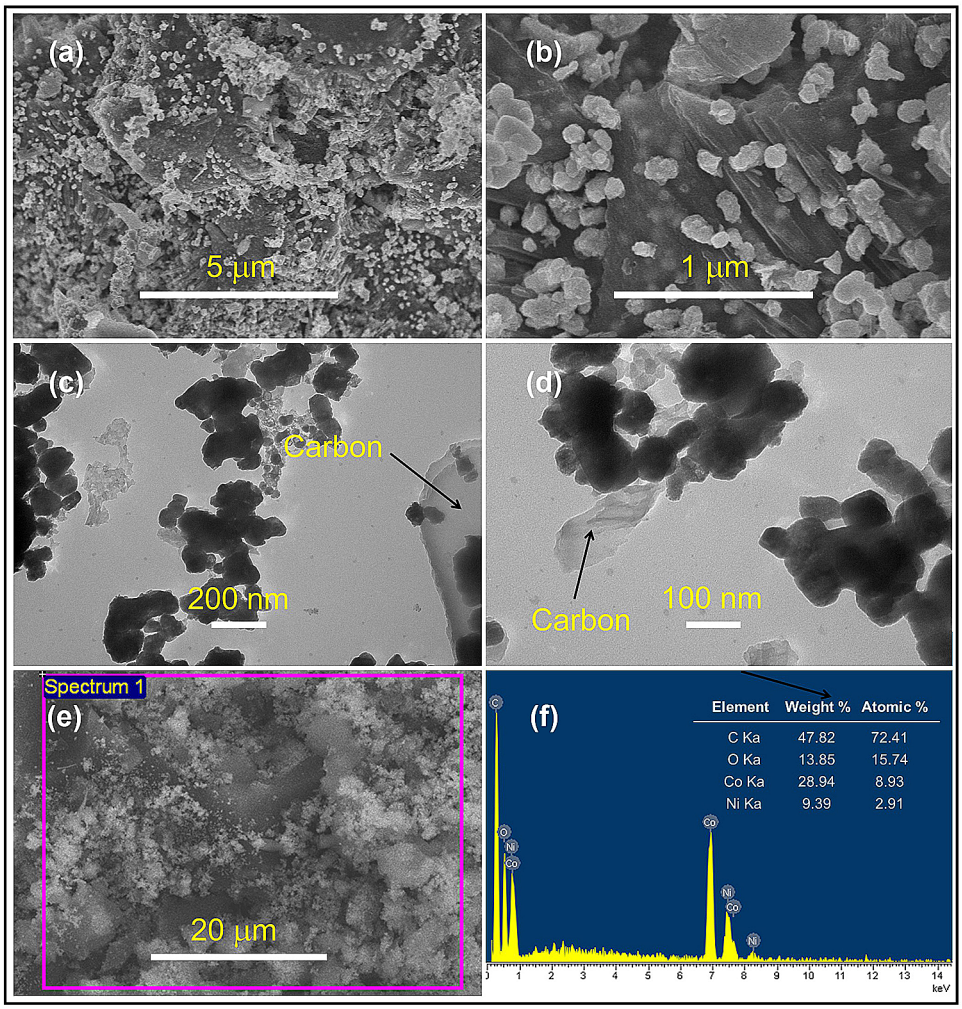

Fig. 3 **a**, **b** SEM images, **c**, **d** TEM images, **e** EDS selected area, **f** EDS spectrum of the $NiCo_2O_4$-amorphous carbon composite

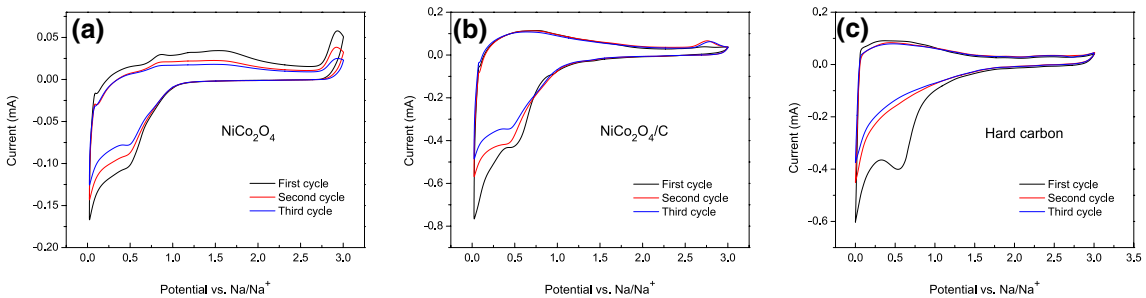

Fig. 4 **a** CV curves of the $NiCo_2O_4$ nanoparticles, **b** CV curves of the $NiCo_2O_4$-amorphous carbon composite, **c** CV curves of the amorphous carbon

$$NiCo_2O_4 + 8Na^+ + 8e^- \rightarrow Ni + 2Co + 4Na_2O \quad (1)$$

$$Ni + Na_2O \leftrightarrow NiO + 2Na + 2e^- \quad (2)$$

$$Co + Na_2O \leftrightarrow CoO + 2Na^+ + 2e^- \quad (3)$$

$$3Co + 4Na_2O \leftrightarrow Co_3O_4 + 8Na^+ + 8e^- \quad (4)$$

As shown in Fig. 4a, for the first cycle, the cathodic peak is located at 0.5 V, which is attributed to the reduction of the NCO to Ni, Co, and amorphous Na_2O (Eq. (1)). In the subsequent two cycles, the cathodic peaks correspond to the reduction of Ni^{2+} to Ni^0. The small anodic peaks at 0.8 V are ascribed to the oxidation of Ni^0 to Ni^{2+} [19, 35, 38]. The

dominant anodic peaks located at 2.9 V of the three cycles are attributed to the oxidation reactions of Co^0 to Co^{3+}.[26]

The CV curves of the NCO/C composite are shown in Fig. 4b. The cathodic peaks of the first three cycles are located at 0.45 V, corresponding to the decomposition of the $NiCo_2O_4$ to Ni, Co, and Na_2O in the first discharging and the reduction of Ni^{2+} to Ni^0 in the next two discharging processes. The anodic peak located at 2.6 V in the first charging process was shifted to 2.8 V in the second and third cycles and the intensity of the peaks increased, suggesting that an activation process occurred for the oxidation reaction of Co/Co^{3+}. The intensity of anodic peaks of the NCO/C composite was smaller than that of NCO nanoparticles (Fig. 4a), indicating that the presence of carbon had reduced the oxidation processes of Ni^0 to Ni^{2+} and of Co^0 to Co^{3+}. The second and third CV curves are well overlapped indicating a reversible electrochemical reaction, displaying a good cycling ability.

Figure 4c shows the CV curves of the amorphous carbon. The broad reduction peak at 0.5 V of the first cycle could be ascribed to the formation of solid electrolyte interface (SEI) on the surface of the carbon electrode [39, 40]. The reduction peak was not observed at the second and the third cycle suggesting that the SEI formation mostly occurred at the first cycle that possibly caused the rapidly faded capacity after the first cycle.

Figure 5a shows the initial three charge/discharge profiles of the NCO-NPs at current density of 50 mA g^{-1} between 0 and 3 V. The discharge capacities of the first to the third cycle were 178 mAh g^{-1}, 142 mAh g^{-1}, and 122 mAh g^{-1}, respectively. The discharge curves show a voltage plateau at 0.5 V, which was consistent to the position of cathodic peaks in the CV curves. The charge curves show a clear voltage plateau at 2.8 V and a small voltage plateau at 0.8 V, corresponding to the dominant anodic and small anodic peaks in the CV curves. The capacity of the NCO-NPs was smaller than that of the reported mesoporous NCO nanosheets [41], hierarchical NCO nanostructure with tunable morphology [38], hollow NCO nanoboxes [19]. This is possibly due to the fact that NCO-NPs morphology is less suitable for Na^+ ions insertion/extraction than the other morphologies.

Figure 5b shows the charge/discharge profiles of the first to third cycles at a current density of 50 mA g^{-1} of the NCO/C composite. The discharge capacities of the first, second, and third were 213 mAh g^{-1}, 205 mAh g^{-1}, and 204 mAh g^{-1}, respectively. The capacity of NCO/C composite was higher than that of the NCO-NPs because the existence of amorphous carbon enhanced the electronic conductivity and some Na^+ ions were possibly accumulated in the amorphous carbon [21, 42]. The charge curves show a clear voltage plateau at 2.8 V, and the second and third charge/discharge profiles are well overlapped. These results are in good agreement with the CV data (Fig. 4b).

The charge/discharge profiles of hard carbon are shown in Fig. 5c. The first discharge capacity of hard carbon (348 mAh g^{-1}) was higher than that of the NCO/C composite. However, the discharge capacity of hard carbon at the second and the third cycle (204 mAh g^{-1} and 192 mAh g^{-1}) was smaller than that of the NCO/C composite. The higher capacity of the NCO/C composite after first cycle compared to the hard carbon could be attributed to the presence of NCO particles on the surface of hard carbon reduced the formation of the SEI. Therefore, the combination of NCO nanoparticles and amorphous carbon took the advantage of high electronic conductivity of carbon and restricted the formation of SEI on the surface of the carbon. As a result, the electrochemical performance of NCO/C composite is better than pristine carbon and NCO nanoparticles.

Figure 6a shows the cycling ability of hard carbon, NCO-NPs, and NCO/C composite at current density of 50 mAh g^{-1} between 0 and 3 V. The first discharge capacity of the NCO-NPs at current density of 50 mA g^{-1} was 172 mAh g^{-1} rapidly decreased to 61 mAh g^{-1} after 10 cycles and then gradually decayed during cycling. After 100 cycles, the capacity of the NCO-NPs remained at 20 mAh g^{-1}. The first discharge capacity of the hard carbon was 348 mAh g^{-1}. The capacity was quickly faded to 198 mAh g^{-1} at the second cycle and then gradually decreased to 43 mAh g^{-1} after 100

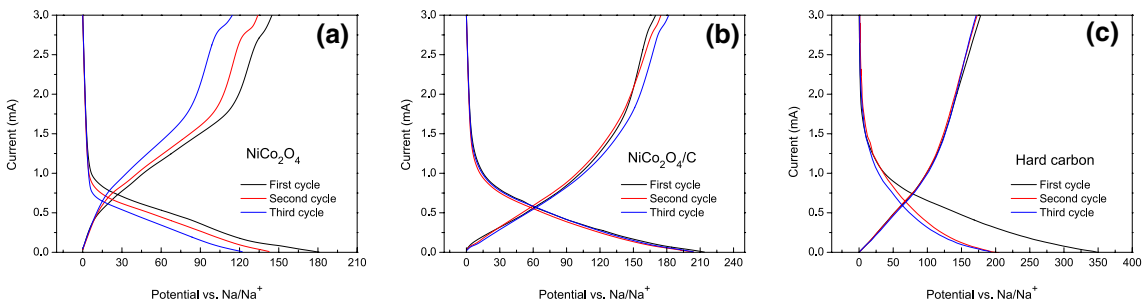

Fig. 5 **a** Charge–discharge profiles of the $NiCo_2O_4$ nanoparticles, **b** charge–discharge profiles of the $NiCo_2O_4$-carbon composite, **c** charge–discharge profiles of the hard carbon

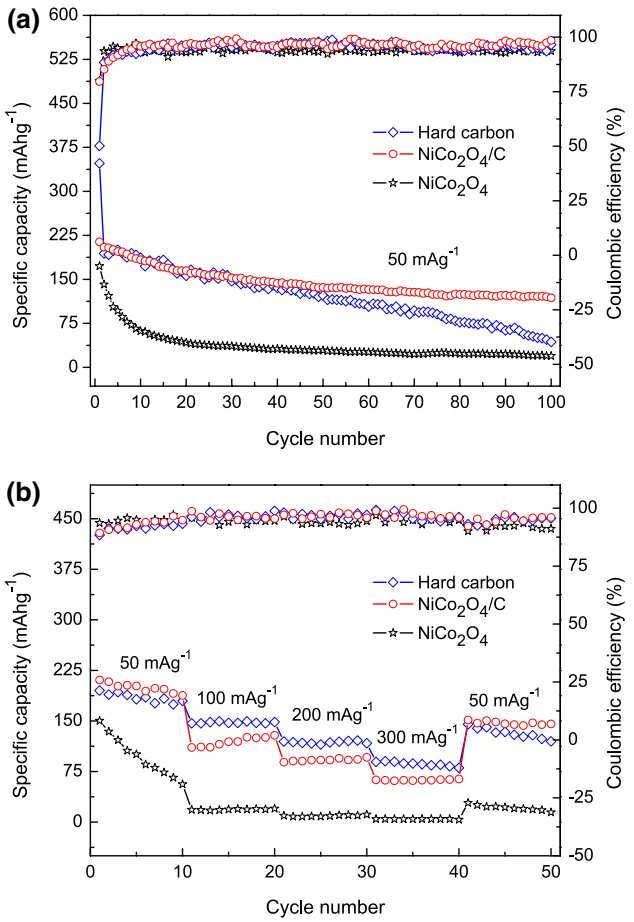

Fig. 6 **a** Cycling ability and Coulombic efficiency of hard carbon, $NiCo_2O_4$ nanoparticles, and $NiCo_2O_4$-amorphous carbon composite at current density of 50 mA g^{-1}, **d** rate capability and Coulombic efficiency of hard carbon, $NiCo_2O_4$ nanoparticles, and $NiCo_2O_4$-amorphous carbon composite

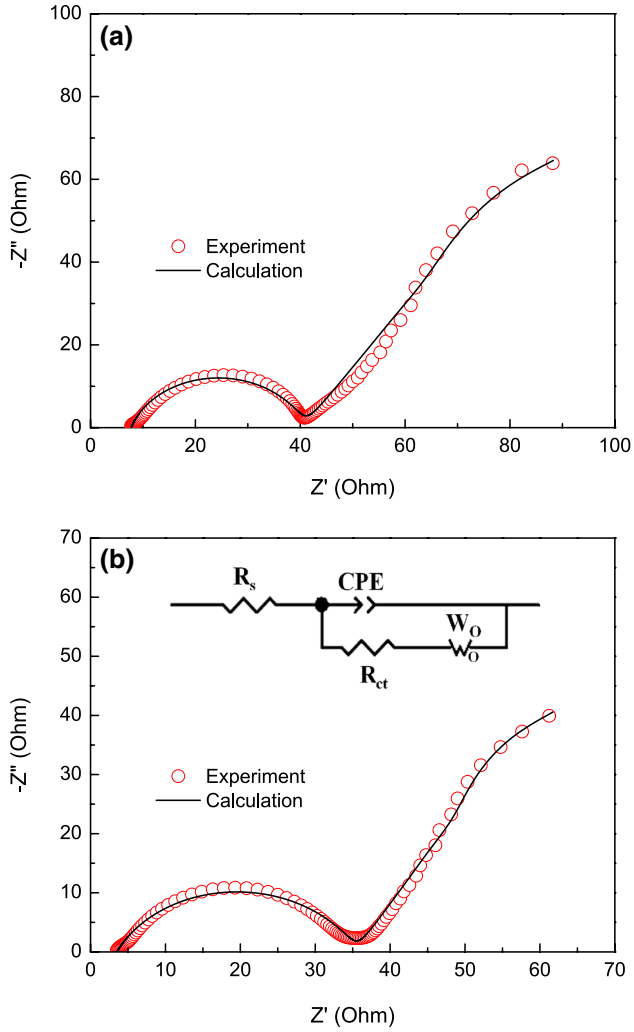

Fig. 7 **a** Electrochemical impedance spectra of as-prepared $NiCo_2O_4$ nanoparticles cell, **b** electrochemical impedance spectra of as-prepared $NiCo_2O_4$-amorphous carbon composite cell and the equivalent circuit used for fitting the EIS experiment data

cycles. The faded capacity of hard carbon at the first cycle was in a good agreement with the CV and charge/discharge data. The first discharge capacity of NCO/C composite was 213 mAh g^{-1}. There was no quickly faded capacity after first cycle observed for NCO/C material. The capacity was slowly decreased and retained of 119 mAh g^{-1} after 100 cycles. The Coulombic efficiency of the hard carbon at the first cycle was of 50%, quickly increased to 88% at the second cycle, and then steadily increased to over 94% after 5 cycles. The Coulombic efficiency of NCO/C composite at the first cycle was 78% and then increased to over 95% after 5 cycles.

The rate capability of hard carbon, NCO-NPs, and NCO/C composite at current densities of 50, 100, 200, and 300 mA g^{-1} from second cycle is shown in Fig. 6b. When the cells cycled at current density of 50 mA g^{-1}, the second discharge capacity of NCO-NPs, hard carbon, and NCO/C composite was about 150, 195, and 210 mAh g^{-1}, respectively. When the current densities increased to 100, 200, and 300 mA g^{-1}, the capacity of hard carbon was higher than that of the NCO-NPs and NCO/C composite due to the higher electronic conductivity of hard carbon. It can be noted that the electrochemical performances of the NCO/C composite were enhanced compared to those of the NCO-NPs due to the profound effect of amorphous carbon in the composite.

The EIS was carried out to provide more insight to the better electrochemical performances of the NCO/C composite than those of the NCO-NPs. Figure 7a, b presents the typical Nyquist plots of the as-prepared NCO-NPs and as-prepared NCO/C composite cells, which were measured in the frequency range of 10^{-2}–10^{6} Hz with amplitude of 30 mV. The two EIS spectra consisted of a semicircle at the high frequency range and an inclined line at the low frequency range. The semicircle is associated with the charge

Table 2 Values of circuit elements in the EIS equivalent circuit

Element	As-prepared $NiCo_2O_4$-NPs cell	As-prepared $NiCo_2O_4$/C cell
R_s (Ω)	7.745	3.512
CPE(C_{dl})-T ($\times 10^{-5}$)	10.4	13.4
CPE(C_{dl})-P	0.8	0.72
R_{ct} (Ω)	33	32
W_o-R	240	145
W_o-T	94	90
W_o-P	0.635	0.67

transfer resistance (R_{ct}) at the electrode–electrolyte interface and the non-homogeneity of the electrode surface represented as a constant phase element (CPE). The left interception of the semicircle with the real axis (Z') indicates the Ohmic resistance (R_s) of the cell. The right interception of the semicircle with the Z' axis represents the ($R_s + R_{ct}$) value. The inclined line is attributed to the Warburg impedance (Wo) of the materials, which represents the diffusion ability of Na^+ ions inside the NCO particles. The EIS spectra of the as-prepared NCO-NPs and as-prepared NCO/C composite cells are similar to those of the NCO materials with different morphologies reported in the literature [17, 19, 37, 38].

The equivalent circuit used to calculate the electrochemical impedances of the materials is shown in the insert of Fig. 7b. The fitted values of the circuit elements of the equivalent circuit are shown in Table 2. The (R_s, R_{ct}) of as-prepared NCO/C composite and NCO-NPs cells are (3.512 Ω, 32 Ω) and (7.745 Ω, 33 Ω), respectively. The Warburg impedance parameters (W_o-R, W_o-T) of the as-prepared NCO/C composite and NCO-NPs cells are (145 Ω, 90) and (240 Ω, 94), respectively. The resistances and the Warburg impedance of the NCO/C composite are smaller than those of the NCO-NPs, which means that the NCO/C composite is favorable to Na^+ ions and electrons transport and subsequently leads to its better electrochemical performances.

4 Conclusions

The NCO-NPs and NCO/C composite were synthesized and electrochemically characterized as the anode materials for the SIBs. It was found that the composite material combining NCO-NPs and amorphous carbon displayed a superior electrochemical performance over the NCO-NPs. This great improvement is assigned to the presence of amorphous carbon of a high electronic conductivity, leading to a high capacity and good cycle ability of the NCO/C material. Our work suggests a new composite material containing amorphous carbon and other anode materials to serve practically as anodes for the SIBs.

Acknowledgements This research was funded by Vietnam National Foundation for Science and Technology Development (NAFOSTED) under Grant Number 103.02-2018.22.

References

1. K. Tang, Y. Wang, X. Zhang, S. Jamil, Y. Huang, S. Cao, X. Xie, Y.S. Wang, Z.C. Luo, G.R. Chen, Electrochim. Acta **312**, 45 (2019)
2. L. Zhang, T. Huang, A. Yu, J. Alloys Compd. **646**, 522 (2015)
3. B. Fu, X. Zhou, Y. Wang, J. Power Sources **310**, 102 (2016)
4. X.F. Zhang, K.X. Wang, X. Wei, J.S. Chen, Chem. Mater. **23**, 5290 (2011)
5. K.T. Lee, T.N. Ramesh, F. Nan, G. Botton, L.F. Nazar, Chem. Mater. **23**, 3593 (2011)
6. S.W. Kim, D.H. Seo, X.H. Ma, G. Ceder, K. Kang, Adv. Energy Mater. **2**, 710 (2012)
7. V.L. Chevrier, G. Ceder, J. Electrochem. Soc. **158**, 1011 (2011)
8. S. Komaba, W. Murata, T. Ishikawa, N. Yabuuchi, T. Ozeki, T. Nakayama, A. Ogata, K. Gotoh, K. Fujiwara, Adv. Funct. Mater. **21**, 3859 (2011)
9. L. Xiao, Y.L. Cao, W.A. Henderson, M.L. Sushko, Y. Shao, J. Xiao, W. Wang, M.H. Engelhard, Z. Nie, J. Liu, Nano Energy **19**, 279 (2016)
10. T. Li, U. Gulzar, X. Bai, S. Monaco, G. Longoni, M. Prato, S. Marras, Z. Dang, C. Capiglia, R.P. Zaccaria, J. Power Sources **384**, 18 (2018)
11. W. Wang, C. Yu, Z. Lin, J. Hou, H. Zhu, S. Jiao, Nanoscale **5**, 594 (2013)
12. N. Arun, V. Aravindan, W.C. Ling, S. Madhavi, J. Alloys Compd. **603**, 48 (2014)
13. Y. Pan, Y. Zhang, B.S. Parimalam, C.C. Nguyen, G. Wang, B.L. Lucht, J. Electroanal. Chem. **799**, 181 (2017)
14. S. Wen, J. Zhao, Y. Zhao, T. Xu, J. Xu, Chem. Phys. Lett. **716**, 171 (2019)
15. L. David, R. Bhandavat, G. Singh, ACS Nano **8**, 1759 (2014)
16. Y. Lu, N. Su, L. Cheng, J. Liu, L. Yang, H. Yang, Q. Yang, S. Li, J. Min, Mater. Lett. **183**, 346 (2016)
17. Y. Wang, H. Huang, Q. Xie, Y. Wang, B. Qu, J. Alloys Compd. **705**, 314 (2017)
18. X. Zhang, Y. Zhou, B. Luo, H. Zhu, W. Chu, K. Huang, Nano-Micro Lett. **10**, 13 (2018)
19. J. Chen, Q. Ru, Y. Mo, S. Hu, X. Hou, Phys. Chem. Chem. Phys. **18**, 18949 (2016)
20. Y. Mo, Q. Ru, J. Chen, X. Song, L. Guo, S. Hu, S. Peng, J. Mater. Chem. A **3**, 19765 (2015)
21. F. Legrain, J. Sottmann, K. Kotsis, S. Gorantla, S. Sartori, S. Manzhos, J. Phys. Chem. C **119**, 13496 (2015)
22. K. Xu, Y. Li, J. Xiong, X. Ou, W. Su, G. Zhong, C. Yang, Front. Chem. **6**, 366 (2018)
23. J. Xu, L. Dong, H. Tang, C. Li, Ceram. Int. **42**, 7803 (2016)
24. L. Zhao, H. Zhao, X. Long, Z. Li, Z. Du, A.C.S. Appl, Mater. Interfaces **10**(42), 35963 (2018)
25. L. Zhao, H. Zhao, Z. Du, J. Wang, X. Long, Z. Lia, K. Świerczek, J. Mater. Chem. A **7**, 9807–9814 (2019)
26. L.N. Zhao, T. Zhang, H.L. Zhaod, Y.L. Hou, Mater. Today Nano **10**, 100072 (2020)
27. O. Knop, K. I. G. Reid, Sutarno, and Y. Nakagawa, Can. J. Chem. **46**, 3463 (1968)

28. K. Park, D. Han, J.K. Shon, S.G. Dooa, S. Lee, RSC Adv. **5**, 6340 (2015)
29. M.Ya. Gamarnik, Phys. Status Solidi B **170**, 27 (1992)
30. A. Mondal, S. Maiti, S. Mahanty, A.B. Panda, J. Mater. Chem. A **5**, 16854 (2017)
31. T. Jiang, X. Wang, S. Tang, J. Zhou, C. Gu, J. Tang, Sci. Rep. **7**, 9795 (2017)
32. D. Zhou, W. Huang, F. Zhao, Solid State Ion. **322**, 18 (2018)
33. D. Su, C. Wang, H. Ahn, G. Wang, Chem. Eur. **19**, 10884 (2013)
34. G. Gao, H.B. Wu, X.W. Lou, Adv. Energy Mater. **4**, 1400422 (2014)
35. Y. Chen, J. Zhu, B. Qu, B. Lu, Z. Xu, Nano Energy **3**, 88 (2014)
36. Y. Mo, Q. Ru, X. Song, S. Hu, L. Guo, X. Chen, Electrochim. Acta **176**, 575 (2015)
37. Y. Wang, P. Liu, K. Zhu, J. Wang, K. Yan, J. Liu, Electrochim. Acta **273**, 1 (2018)
38. F. Fu, J. Li, Y. Yao, X. Qin, Y. Dou, H. Wang, J. Tsui, K. Chan, M. Shao, A.C.S. Appl, Mater. Interfaces **9**, 16194 (2017)
39. K. Tang, L.J. Fu, R.J. White, L.H. Yu, M.M. Titirici, M. Antonietti, J. Maier, Adv. Energy Mater. **2**, 873 (2012)
40. K. Hong, L. Qie, R. Zeng, Z. Yi, W. Zhang, D. Wang, W. Yin, C. Wu, Q. Fan, W. Zhang, Y. Huang, J. Mater. Chem. A **2**, 12733 (2014)
41. K. Zhou, Z. Hong, C. Xie, H. Dai, Z. Huang, J. Alloys Compd. **651**, 24 (2015)
42. S. Li, J. Qiu, C. Lai, M. Ling, H. Zhao, S. Zhang, Nano Energy **12**, 224 (2015)